Three-dimensional buoyancy-induced flow and heat transfer around the wheel outboard of an aircraft

C. Desai and K. Vafai
Department of Mechanical Engineering, The Ohio State University, Columbus, OH, USA

Three-dimensional buoyancy-driven flow and heat transfer in an annular cavity with an end open to the ambient surroundings were numerically simulated. This geometry finds direct application in the wheel outboard portion of an aircraft brake housing and plays an important role in the thermal performance of the brake housing assembly. The virtually unknown boundary conditions at the open end were implemented by making use of an extended computational domain at the open end. The numerical scheme used in the present study is based on the Galerkin method of finite element formulation. A number of interesting features of the flow and heat transfer fields resulting from the sudden heating of the inner cylinder were studied in detail. Results including the local and average Nusselt numbers were obtained for a wide range of Rayleigh numbers, and it was found that the physics of the flow changes considerably at high Rayleigh numbers. The effect of the length of the inner cylinder on the flow field and the heat transfer coefficients were studied thoroughly. The validity of the numerical code used is ascertained by comparing results for some pertinent annular geometries with previously published results.

Keywords: natural convection; three-dimensional; laminar; open end boundary; finite element

Introduction

Buoyancy-induced flow and heat transfer in an annulus bounded by horizontal, coaxial cylinders has been an area of great interest to investigators in recent years. This is primarily because several domains of practical interest, such as nuclear reactors, thermal storage systems, and electric transmission cables, can be approximated by various extensions of this type of geometry. Detailed numerical and experimental studies related to this geometry have been carried out by previous researchers.[1–3] These studies made use of a two-dimensional (2-D) model, which is valid only when the annulus is infinitely long so that convection can be assumed to be confined in the transverse plane and the axial gradients of all variables can be ignored. However, when the annulus has a finite length, as well as in cases where the cylinder is inclined with respect to the horizontal, because of the flow retardation caused by the end walls, a full three-dimensional (3-D) analysis of the problem is necessary.

In the 3-D numerical analysis, the system of equations to be solved is larger and much more complex than the 2-D case, taking more CPU time and memory to obtain the solution. In the past decade, investigators have carried out 3-D numerical studies of buoyancy-driven flow in a cylindrical annulus. Ozoe et al.[4] modified the vorticity vector potential approach for application in cylindrical polar coordinates to solve the natural convection problem for a vertical annulus heated from below. The circulation pattern was found to be a symmetrical set of roll cells, with their axes in the radial direction and in a single horizontal plane. In later work, Ozoe et al.[5] made an experimental and numerical investigation to study the effects of inclination for the same problem. Takata et al.[6] performed a complete analytical and experimental investigation of natural convection in an inclined cylindrical annulus enclosed between heated inner and cooled outer cylinders. Three-dimensional governing equations, in terms of vorticity and vector potential, were transformed into the finite-difference equations and solved numerically using the successive over-relaxation procedure. This spiral flow pattern was further confirmed in the 3-D numerical analysis made by Fusegi and Farouk[7] for a horizontal cylindrical annulus of small length, using a vorticity-velocity formulation.

Rao et al.[8] carried out a numerical study of 3-D natural convection in a horizontal porous annulus heated from the inner surface, by using the Galerkin formulation of the finite element method. They further clarified the spiral structure of the flow. The most recent study on natural convection in a horizontal annulus has been made by Fukuda et al.[9] They made a direct numerical simulation of the turbulent natural convection regime using an explicit leapfrog scheme.

Though some studies have been carried out on the numerical simulation of 3-D natural convection in annuli with finite length and solid end walls, an interesting phenomenon of buoyancy-driven flow in an annular cavity with an open end has only very recently received some attention. One of the main characteristics of the buoyancy-induced flows in the open or partially open cavities is its basic geometry, which among other aspects, reveals the interactions and the influence of the inner (inside the cavity) and the outer (the open region) flow and

Address reprint requests to Professor Vafai at the Department of Mechanical Engineering, The Ohio State University, Columbus, OH 43210, USA.

Received 6 May 1991; accepted 17 August 1991

temperature fields. There has been very little work done on these type of interactions, which can occur in various practical applications. Aside from constituting a fundamental area of research in heat transfer, understanding these inner and outer interactions will allow us to obtain a better understanding of a number of practical applications such as various aircraft brake housing systems where the wheel outboard of the brake housing of an aircraft can be modeled around this basic geometry. The brake housing assembly of an aircraft partly interacts with the surroundings through the wheel outboard portion. The axle tip is the hot inner cylinder in the model and is the part that dissipates heat to the surroundings from the inner parts of the brake housing. The annular cavity of interest here is the portion between the axle tip and the wheel rim on which the tire is mounted. The interaction between the fluid inside the cavity and the outside domain has a direct influence on the fluid mechanics and heat transfer of the buoyancy-induced flow inside the annulus. A thorough understanding of the natural convection process in this geometry provides a strong basis for predicting and maximizing the convective energy transfer from the brake housing to the surrounding.

The main difficulty associated with the study of fluid flow in open-ended structures is the specification of boundary conditions at the open end. Numerical studies of natural convection in open-ended rectangular cavities using a 2-D model have been carried out by investigators in the past. Most of these studies have included computations in an extended computational domain,[10,11] thus partially overcoming the problem of unknown physical conditions at the opening. It has been shown[12,13] that the extent of the enlarged computational domain has a much more pronounced effect on the results than those anticipated by previous researchers. Chan and Tien[14] performed a numerical study of natural convection in 2-D rectangular shallow open cavities by a simpler approach of restricting the computations within the cavity.

The present study focuses attention on the numerical simulation of the transient, 3-D process of buoyancy-induced flow and heat transfer in a partially open annular cavity bounded by a hot inner cylinder, cold outer cylinder, and an insulated end wall. To study the interaction between the fluid inside the annular space and that in the ambient surrounding, the boundary conditions at the open end are taken care of by making use of an extended computational domain. The numerical procedure used in this work for solving the full 3-D Navier-Stokes equations is based on the Galerkin weighted residual method of finite element formulation. The highly nonlinear set of discretized equations are solved by using a quasi-Newton method. All the results presented here are obtained by using the fluid dynamics analysis package (FIDAP), a general purpose finite element code for incompressible flows. Detailed results for fluid flow and heat transfer effects over a range of Rayleigh numbers are presented.

Analysis

Physical model and assumptions

The physical model and coordinate system used here are shown in Figure 1. The fluid is bounded by the inner cylinder of outer radius R_1 and the outer cylinder of inner radius R_2. The lengths of these cylinders are L_1 and L_2, respectively. One end of the annulus is rigid and insulated while the other end is open to the ambient surrounding. The annulus is placed horizontally and gravity is confined to the negative x-direction. The temperature and flow fields are assumed to be symmetrical with

Notation

c_p	Heat capacity
g	Acceleration due to gravity, ms^{-2}
k	Thermal conductivity
L_1	Length of the inner cylinder, m
L_2	Length of the outer cylinder, m
L_3	Length of the extended computational domain, m
Nu	Nusselt number
n	Outward normal to a surface
Pr	Prandtl number, ν/α
p	Pressure (Pa)
p^h	FEM approximation for pressure
R_1	Radius of the inner cylinder, m
R_2	Radius of the outer cylinder, m
R_3	Radius of the extended computational domain, m
Ra	Rayleigh number, $g\beta R_2^3 \Delta T/\nu\alpha$
t	Time, s
T	Temperature, K
T^h	FEM approximation for temperature
u_x	Velocity in the x-direction, ms^{-1}
u_y	Velocity in the y-direction, ms^{-1}
u_z	Velocity in the z-direction, ms^{-1}
u_x^h	FEM approximation for the x-component of velocity
u_y^h	FEM approximation for the y-component of velocity
u_z^h	FEM approximation for the z-component of velocity
V	Column vector consisting of all the unknown variables in the computational domain (u_x, u_y, u_z, p, T)
x, y, z	Cartesian coordinates, m

Greek symbols

α	Thermal diffusivity
β	Coefficient of volume expansion
μ	Kinematic viscosity, $kg\,m^{-1}\,s^{-1}$
ν	Dynamic viscosity, $m^2\,s^{-1}$
ρ	Density, $kg\,m^{-3}$

Subscripts

1	Inner cylinder
2	Outer cylinder
3	Far-field condition for the extended computational domain
x	x-component
y	y-component
z	z-component
∞	Condition at infinity

Superscripts

T	Transpose of a matrix

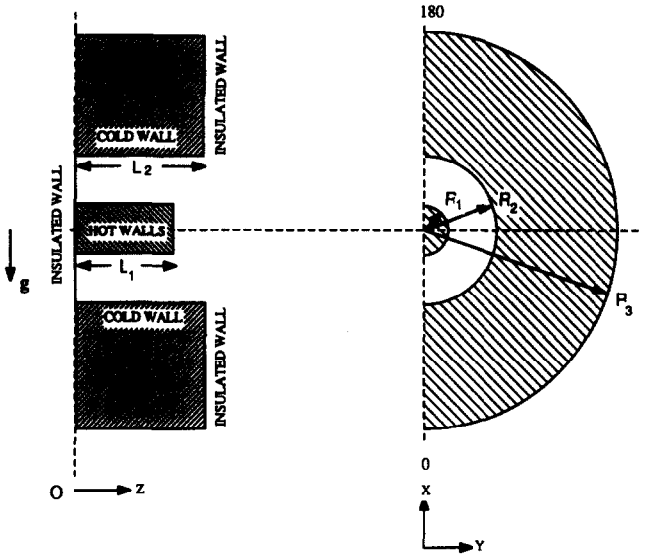

Figure 1 Schematic representation of a partially open annular cavity

respect to the vertical plane, which passes through the cylinder centers and, as a result, the region of interest is only half the annulus, as shown in the figure. It is assumed in the analysis that the thermophysical properties of the walls and the fluid are independent of temperature except for the density in the buoyancy term. The fluid is Newtonian, incompressible, and the Boussinesq approximation is valid. Viscous heat dissipation in the fluid is negligible in comparison to conduction and convection.

Model equations

The problem is modeled as the 3-D, transient, natural convection in an incompressible fluid. The Boussinesq approximation allows a simplification for density in the gravitational body force term, which causes the buoyancy force necessary to drive the flow. The equations describing the motion are the full, 3-D Navier-Stokes equations, written here in nondimensional form using Cartesian coordinates:

Continuity

$$\frac{\partial u_x}{\partial x}+\frac{\partial u_y}{\partial y}+\frac{\partial u_z}{\partial z}=0 \tag{1}$$

x-momentum

$$\left(\frac{\mathrm{Ra}}{\mathrm{Pr}}\right)^{1/2}\left\{\frac{\partial u_x}{\partial t}+u_x\frac{\partial u_x}{\partial x}+u_y\frac{\partial u_x}{\partial y}+u_z\frac{\partial u_x}{\partial z}\right\}=-\frac{\partial p}{\partial x}+\left(\frac{\mathrm{Ra}}{\mathrm{Pr}}\right)^{1/2}T+\frac{\partial^2 u_x}{\partial x^2}+\frac{\partial^2 u_x}{\partial y^2}+\frac{\partial^2 u_x}{\partial z^2} \tag{2}$$

y-momentum

$$\left(\frac{\mathrm{Ra}}{\mathrm{Pr}}\right)^{1/2}\left\{\frac{\partial u_y}{\partial t}+u_x\frac{\partial u_y}{\partial x}+u_y\frac{\partial u_y}{\partial y}+u_z\frac{\partial u_y}{\partial z}\right\}=-\frac{\partial p}{\partial y}+\frac{\partial^2 u_y}{\partial x^2}+\frac{\partial^2 u_y}{\partial y^2}+\frac{\partial^2 u_y}{\partial z^2} \tag{3}$$

z-momentum

$$\left(\frac{\mathrm{Ra}}{\mathrm{Pr}}\right)^{1/2}\left\{\frac{\partial u_z}{\partial t}+u_x\frac{\partial u_z}{\partial x}+u_y\frac{\partial u_z}{\partial y}+u_z\frac{\partial u_z}{\partial z}\right\}=-\frac{\partial p}{\partial z}+\frac{\partial^2 u_z}{\partial x^2}+\frac{\partial^2 u_z}{\partial y^2}+\frac{\partial^2 u_z}{\partial z^2} \tag{4}$$

Energy

$$(\mathrm{RaPr})^{1/2}\left\{\frac{\partial T}{\partial t}+u_x\frac{\partial T}{\partial x}+u_y\frac{\partial T}{\partial y}+u_z\frac{\partial T}{\partial z}\right\}=\frac{\partial^2 T}{\partial x^2}+\frac{\partial^2 T}{\partial y^2}+\frac{\partial^2 T}{\partial z^2} \tag{5}$$

We have used the following dimensionless parameters and dropped the superscripts for convenience:

$$x^*=\frac{x}{R_2}\qquad y^*=\frac{y}{R_2}\qquad z^*=\frac{z}{R_2}$$

$$u_x^*=\frac{u_xR_2}{\alpha(\mathrm{RaPr})^{1/2}}\qquad u_y^*=\frac{u_yR_2}{\alpha(\mathrm{RaPr})^{1/2}}\qquad u_z^*=\frac{u_zR_2}{\alpha(\mathrm{RaPr})^{1/2}}$$

$$T^*=\frac{T-T_s}{T_1-T_s}\qquad p^*=\frac{pR_2^2}{\mu\alpha(\mathrm{RaPr})^{1/2}}\qquad t^*=\frac{t\alpha(\mathrm{RaPr})^{1/2}}{R_2^2}$$

These five equations in terms of five unknowns, along with the appropriate initial and boundary conditions, fully describe the transient, convective energy transfer process in a partially open annular cavity.

Initial conditions

All the walls of the annulus are assumed to be at uniform, ambient temperature initially and the fluid is assumed to be stagnant and at ambient temperature throughout the computational domain. Thus, we have

At $t=0$

$$u_x=u_y=u_z=T=0 \tag{6}$$

Boundary conditions

We have made use of an extended computational domain for implementing the virtually unknown boundary conditions at the open end. A sketch of the computational domain is depicted in Figure 2. As shown in the figure, the different boundaries encountered in the present study can be categorized as (1) rigid boundaries, (2) symmetry boundaries, and (3) open boundaries.

Rigid boundaries. On all the rigid, impermeable boundaries in the computational domain, the no-slip boundary condition for velocity is applied. All the surfaces of the inner cylinder are assumed to be maintained at a uniform dimensionless temperature of T_1. The inner curved surface of the outer cylinder is maintained at the temperature of the surrounding, T_2. The vertical walls of the outer cylinder and the closed end wall of the annulus are assumed to be insulated. Following the same numbering as in Figure 2, we have

(1) For the axial end wall of the annulus

At $z=0$ and $\dfrac{R_1}{R_2}\leqslant r\leqslant 1$,

$$u_x=u_y=u_z=0,\qquad \frac{\partial T}{\partial z}=0 \tag{7}$$

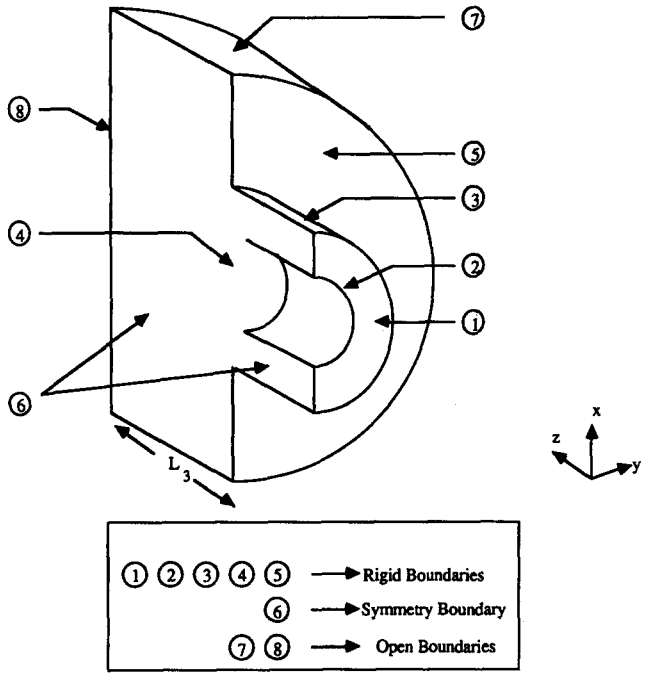

Figure 2 Extended computational domain used for the present study

(2) For the curved surface of the inner cylinder

$$\text{At } r = \frac{R_1}{R_2} \text{ and } 0 \leqslant z \leqslant \frac{L_1}{R_2},$$

$$u_x = u_y = u_z = 0, \qquad T = T_1 \tag{8}$$

(3) For the curved surface of the outer cylinder

$$\text{At } r = 1 \text{ and } 0 \leqslant z \leqslant \frac{L_2}{R_2},$$

$$u_x = u_y = u_z = 0, \qquad T = T_2 \tag{9}$$

(4) For the vertical (flat) surface of the inner cylinder

$$\text{At } z = \frac{L_1}{R_2} \text{ and } 0 \leqslant r \leqslant \frac{R_1}{R_2},$$

$$u_x = u_y = u_z = 0, \qquad T = T_1 \tag{10}$$

(5) For the vertical (flat) surface of the outer cylinder

$$\text{At } z = \frac{L_2}{R_2} \text{ and } 1 \leqslant r \leqslant \frac{R_3}{R_2},$$

$$u_x = u_y = u_z = 0, \qquad \frac{\partial T}{\partial z} = 0 \tag{11}$$

Symmetry boundaries. Since there is no flow exchange between the two halves of the annulus across the vertical symmetry (x-z) plane, the normal component of velocity at this plane is taken to be zero. Therefore, symmetry conditions with respect to the vertical plane, which divides the annulus into two halves, are used. The symmetry boundary condition was verified by comparing the results for the full geometry with those for the half annulus at several Rayleigh numbers. The gradients of all variables other than the normal component of velocity in the normal direction at the symmetry plane are specified to be zero. This can be written as

(6) For the symmetry plane

$$u_y = 0, \qquad \frac{\partial u_x}{\partial y} = \frac{\partial u_z}{\partial y} = \frac{\partial T}{\partial y} = 0 \tag{12}$$

Permeable boundaries. As mentioned before, the main difficulty involved in the numerical simulation of the flow field and heat transfer in open-ended structures is the specification of the boundary conditions at the open end. Since it is virtually impossible to impose appropriate boundary conditions at the open end without overconstraining the problem, the simulation should include calculations in an extended computational domain. This extension not only takes care of the open boundary conditions but also aids in understanding the complex coupling effects between the fluid in the cavity and the ambient surrounding. In the present study, the extension is a cylinder of radius R_3 and length L_3. The choice of these dimensions is made such that further extension will not have a significant effect on the temperature and flow fields inside the annulus and near the opening. In the present investigation, two choices were possible to approximate the boundary conditions at the far field, namely

(i) $\zeta = 0$

(ii) $\dfrac{\partial \zeta}{\partial n} = 0$

where, in the above equations, ζ stands for either u_x, u_y, u_z, or T and n is the coordinate normal to the boundary. The first choice is physically justified by the fact that all the variables should diminish at the far-field boundaries in the limiting case when these boundaries are at a very large distance from the open end. But this would result in a substantial increase in the number of elements and, hence, a large increase in computational costs. The second choice was found to be a good approximation of the far-field conditions without the necessity for an excessively large computational domain. Therefore, in the present work, the conditions at the far field are represented by setting the gradients of temperature and of the three components of the velocity in the normal direction equal to zero. This is a better approximation than that used by previous investigators,[10,11] who have set the tangential components of velocity at the far-field boundary equal to zero along with zero values for the normal temperature gradients and the gradient of the normal velocity. Their computations were carried out in an extended computational domain, with maximum dimensions only about twice those of the cavity. However, these dimensions were found to be substantially inadequate by Ettefagh and Vafai,[12,13] who showed that an extension of at least 16 times the cavity dimensions was necessary to eliminate the effects of the far field. Also, the constraint of zero tangential velocity at the boundaries of the extension was eliminated in their study. Our present representation of the open boundary conditions is a good one because it removes the constraint of zero tangential velocity at the far field. Also, the boundary conditions applied at the end of the extension give a good representation of the far field, without the requirement of a very large extension and without sacrificing the accuracy of the solution obtained. These far-field boundary conditions can be stated as

(7) For the open radial boundary of the extended computational domain

$$\text{At } r = \frac{R_3}{R_2} \text{ and } 0 \leqslant z \leqslant \frac{L_3 + L_2}{R_2},$$

$$\frac{\partial u_x}{\partial n} = \frac{\partial u_y}{\partial n} = \frac{\partial u_z}{\partial n} = 0, \qquad \frac{\partial T}{\partial n} = 0 \tag{13}$$

(8) For the open axial boundary of the extended computational domain

$$\text{At } z = \frac{L_3 + L_2}{R_2} \text{ and } 0 \leqslant r \leqslant \frac{R_3}{R_2},$$

$$\frac{\partial u_x}{\partial z} = \frac{\partial u_y}{\partial z} = \frac{\partial u_z}{\partial z} = 0, \qquad \frac{\partial T}{\partial z} = 0 \tag{14}$$

This completes the formulation of the problem. The solution of the set of governing equations along with the specified boundary conditions give the flow and temperature fields associated with the convective energy transfer process in the partially open annulus. Since the equations are too complex to be solved analytically, a numerical procedure has been used for the solution. The numerical scheme is explained in the following section.

Numerical scheme

A Galerkin-based finite element method was employed to solve the system of differential equations described in the previous section. The application of this technique is well described by Taylor and Hood[15] and Gresho et al.,[16] and its application in the finite element code used in the present work is also well documented.[17] This scheme is briefly explained here.

The continuum domain is first divided into a set of simply shaped, nonoverlapping regions called elements, within each of which the unknown variables u_x, u_y, u_z, p, and T are approximated by using the following equations:

$$u_x \approx u_x^h = \phi^T[U_x] \tag{15a}$$

$$u_y \approx u_y^h = \phi^T[U_y] \tag{15b}$$

$$u_z \approx u_z^h = \phi^T[U_z] \tag{15c}$$

$$p \approx p^h = \psi^T[P] \tag{15d}$$

$$T \approx T^h = \theta^T[T] \tag{15e}$$

where ϕ, ψ, and θ are the interpolation functions for velocity, pressure, and temperature, respectively, and are local functions of the nodal coordinates for that element as well as the independent variables. The vectors $[U_x]$, $[U_y]$, $[U_z]$, $[P]$, and $[T]$ consist of the values of the respective variables at the nodes of the element.

Substituting these basis functions into the governing equations and boundary conditions yields a residual (error) in each of the equations. This can be stated as follows:

$$\textit{Continuity} \quad f_1(\phi, U_x, U_y, U_z) = E_1 \tag{16a}$$

$$\textit{Momentum} \quad f_2(\phi, \psi, \theta, U_x, U_y, U_z, P, T) = E_2 \tag{16b}$$

$$\textit{Energy} \quad f_3(\phi, \theta, U_x, U_y, U_z, T) = E_3 \tag{16c}$$

where E_1, E_2, and E_3 are the residuals (errors) resulting from the use of the finite element approximations.

The Galerkin form of the method of weighted residuals seeks to reduce these errors to zero in a weighted sense, i.e., by making the residuals orthogonal to the interpolation functions of each element. These orthogonality conditions are expressed by

$$\int_V \psi \cdot E_1 \, dV = \int_V \psi \cdot f_1 \, dV = 0 \tag{17a}$$

$$\int_V \phi \cdot E_2 \, dV = \int_V \phi \cdot f_2 \, dV = 0 \tag{17b}$$

$$\int_V \theta \cdot E_3 \, dV = \int_V \theta \cdot f_3 \, dV = 0 \tag{17c}$$

This procedure yields a stream of equations for each element, which can be written as

$$\bar{M} \frac{\partial V}{\partial t} + \bar{K}(V) \cdot V = \bar{F} \tag{18}$$

where

V = column vector of the unknown variables
F = force vector (incorporating the boundary conditions)
M = mass matrix
K = stiffness matrix (representing the diffusion and convection of energy)

The above equation represents the discrete analogue of the governing continuum Equations 1–5 for an individual fluid element. The discrete representation of the entire continuum region of interest is obtained through an assemblage of elements such that interelement continuity of velocity and temperature is enforced. The result of such an assembly process is a system of matrix equations of the form given by Equation 18.

To obtain a transient solution, the continuous time derivative needs to be replaced by an approximation for the history of the time-dependent variable over a small portion of the problem time scale. In other words, some sort of a time integration scheme is necessary. The result is an incremental procedure that advances the solution in discrete steps of time. The trapezoidal scheme developed by Gresho et al.[16] was used for the time discretization of the governing equations. By an appropriate combination of two common, second-order accurate integration techniques, the implicit trapezoidal rule and an explicit Adams-Bashforth formula, they developed a stable time integration scheme in which the size of the time step can be optimally varied, based solely on temporal accuracy requirements.

Since an implicit time integrator has been used in the present case for discretization of the governing equations in time, at each time step, a nonlinear system of equations needs to be solved. Gresho et al.[16] showed that with the predictor-corrector scheme used in the present code, if the user-specified local time truncation error tolerance is set to 0.001–0.005, i.e., 0.1–0.5 percent error, then the predictor is sufficiently accurate that only one Newton-Raphson iteration is required at each time step to achieve convergence. However, this can still be inefficient in studies like the present for which even one iteration can take a considerable amount of CPU time when the Newton-Raphson method is used. To reduce this time, we have used the quasi-Newton solution algorithm to solve the nonlinear system at each time step. This algorithm can be shown to be superlinearly convergent and, in practice, its convergence rate approaches that of the Newton-Raphson, while the time for one iteration of quasi-Newton is typically 10–20 percent of the time for a Newton-Raphson iteration. A complete description of this quasi-Newton method in the FEM simulation of incompressible fluid flows is given by Engelman et al.[18]

The advantage of the quasi-Newton method in the framework of the transient algorithm is that now the reformation of the Jacobian matrix need only be performed every N time steps. Of course, a balance must be found between the number of steps N and the quasi-Newton iterations required at each time step to achieve convergence. Typically, if $N = 2$ or 3, a savings in computer time of the order of 50 percent over the one-step Newton-Raphson method can be attained.

Validity of the numerical code

The validity and accuracy of the numerical scheme used for the present analysis was verified by considering the natural convection process in a 2-D annulus and a 3-D annulus with closed-end walls. These cases provide reliable

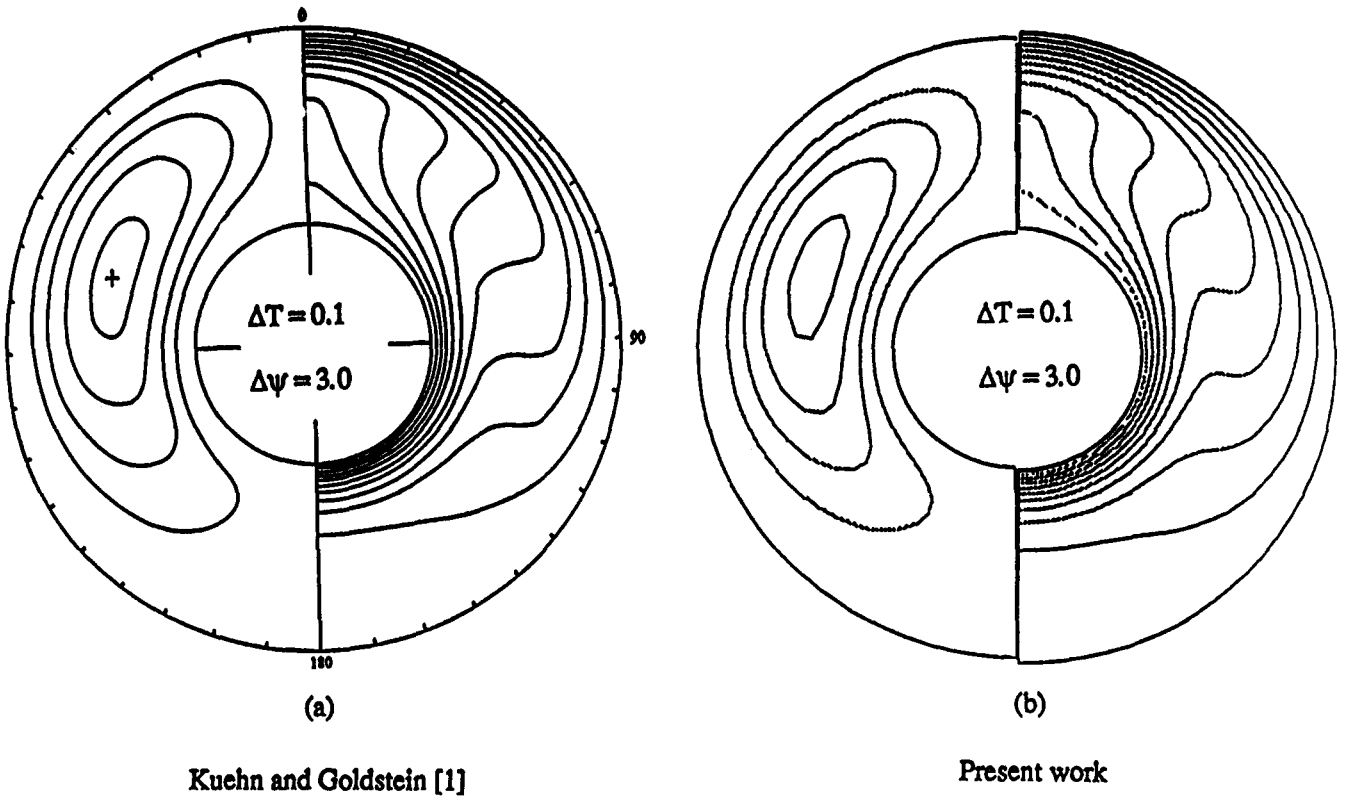

Figure 3 Comparison of streamlines and isotherms for 2-D annuli. Ra = 10^4, Pr = 0.7

information for studying the accuracy and feasibility of using the finite element method for our study. Results are presented here showing in detail a quantitative and qualitative comparison of the flow and temperature fields.

Comparison of results for two-dimensional annuli

We have used the results obtained by Kuehn and Goldstein[1] for a 2-D annulus for benchmarking our results in the first case. Their work consisted of an experimental investigation as well as a steady-state 2-D finite difference numerical simulation of natural convection in a horizontal concentric annulus. The computations were carried out for an annulus with a radius ratio of 2.6 and using air (Pr = 0.7) and water (Pr = 5) as working fluids. Streamlines and isotherms obtained by FIDAP are presented along with the results of Kuehn and Goldstein[1] in Figure 3. Comparison of the results clearly illustrates that the two methods give the same solution. Even the magnitudes of the streamlines are in good agreement, as shown. The agreement between the results can also be seen by the fact that the centers of rotation of the recirculating vortex obtained by the two methods are located at the same position. Furthermore, a comparison of the mean Nusselt numbers at the inner and outer cylinders obtained showed agreement within 1 percent.

Comparison of results for three-dimensional closed annuli

An in-depth study of the 3-D buoyancy-induced flow in an annulus bounded by horizontal, coaxial cylinders and with closed ends was carried out by Vafai and Ettefagh.[19] They performed a numerical simulation using a vorticity-vector potential method for an annulus with a radius ratio of $R_2/R_1 = 2.6$ and length to outer cylinder radius ratio of $L/R_2 = 4$. Calculations were performed for Rayleigh numbers of 4.3×10^3 and 4.3×10^4 using air (Pr = 0.7) as the working fluid.

Table 1 Comparison of flow field results for Ra = 4.3×10^3 (closed annulus)

	Maximum value of the velocity vector in the radial plane		
Axial position	FDM	FEM	Difference (%)
L/40	8.56	8.71	1.70
L/8	12.75	12.81	1.25
L/2	13.17	13.31	0.90

For the Rayleigh number of 4.3×10^3, the isotherms are slightly eccentric circles (not shown here), indicating the presence of a very weak convective flow. The end wall effects in this case are negligible, and the core region in which the flow field is essentially 2-D is very long, extending almost throughout the entire length of the cylinder. The axial component of velocity exists in regions close to the end wall, thus indicating the presence of a 3-D flow field. The magnitude of the axial velocities is very low compared with the velocity vectors in the radial plane. A comparison of the velocity magnitudes obtained from the present case and those obtained by Vafai and Ettefagh[19] is given in Table 1. Also, contours of the axial component of velocity in two planes located very close to the end walls are shown in Figure 4. The convention used in the contours for the present work is that the dotted lines indicate a positive axial velocity whereas the solid contour lines indicate the negative values of the axial velocity. The convention used by Vafai and Ettefagh[19] is exactly the opposite. From the

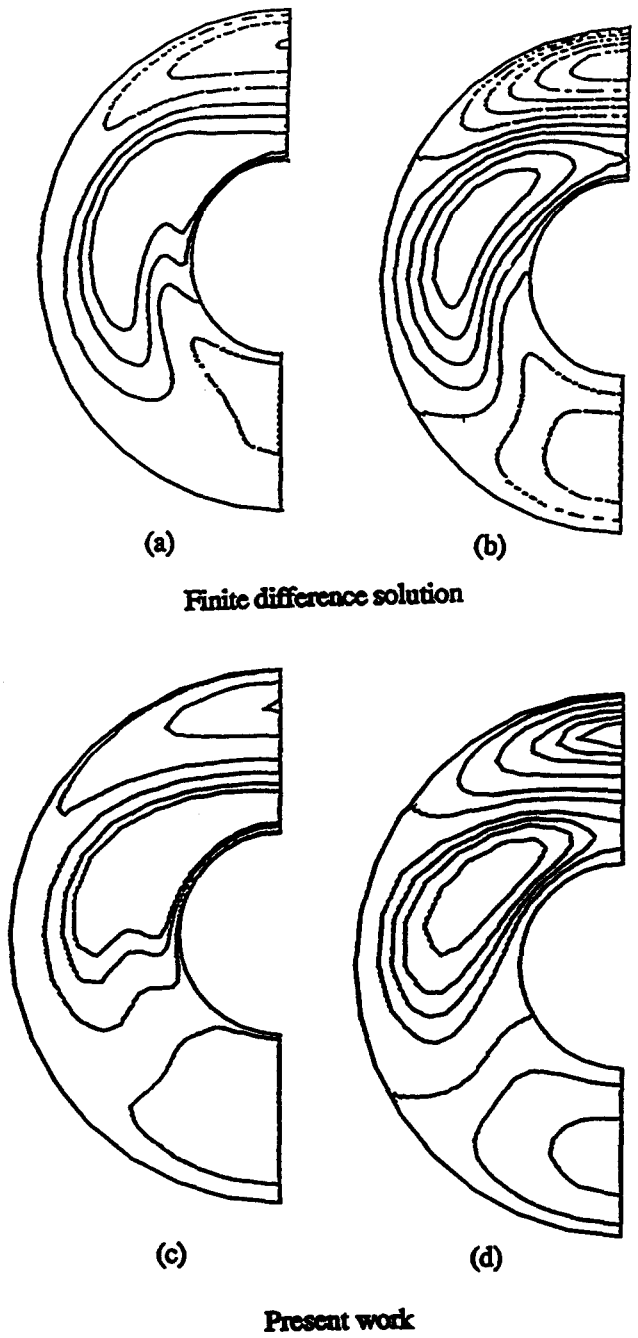

Figure 4 Comparison of axial velocity contours for the closed annulus ($Ra = 4.3 \times 10^3$) at different locations. (a) and (c) $z = L/40$; (b) and (d) $z = L/8$

values given and also from the figure, it can be seen that our results are in good agreement with those presented by the previous investigators. The minor qualitative discrepancy in the axial velocity contours can be attributed to the inherent differences between the finite difference and finite element techniques used for the solution of the problem. The mean Nusselt numbers over the inner and outer cylinder surfaces at the top angular plane are given in the Table 2. From the values shown, we see that our results fall within 1.7 percent of the finite difference results.

The isotherms at the midaxial plane and the end wall of the annulus as predicted by Vafai and Ettefagh[19,20] for $Ra = 4.3 \times 10^4$ are shown in Figure 5. The figure also shows the isotherms at the same locations obtained using the finite element algorithm. Comparison of these isotherms shows good agreement between the two results. The clustering of isotherms around the inner and outer cylinders at the mid-axial plane is a result of the higher strength of the recirculating flow in that region. The retardation caused by the end wall causes a reduction in velocities and hence, the clustering effect of the isotherms at the inner and outer cylinders diminishes.

Results obtained by Takata et al.[6] were also used to compare the solutions for the 3-D closed annulus. The numerical computations performed by these investigators were for an annulus with a radius ratio $R_2/R_1 = 2$ and length to outer cylinder radius ratio $L/R_2 = 2$. The Rayleigh number of the flow was 10^5 and the Prandtl number of the fluid used was 5000. Only one Prandtl number was used, and the investigators only concentrated on the steady-state solution of the problem. It appears that the high Prandtl number fluid was necessary in their case to result in stability for their numerical scheme. Isotherms at the mid-axial plane and the end wall of the annulus at steady state are shown in Figure 6. The isotherms at the same locations using finite element results are also shown in the figure. From the figure, it can be seen that the results obtained using the finite element method (present work) are in good agreement with the results of Takata et al.[6] Comprehensive comparative differences between the finite element and finite difference methods for three-dimensional natural convection problems in closed and open-ended cavities are given by Vafai and Desai.[21]

Results and discussion

Results presented here are for a hot outer surface of the inner cylinder ($T_1 = 1$), a cold inner surface of the outer cylinder ($T_2 = 0$), and using air as the working fluid ($Pr = 0.7$). The annulus considered has a radius ratio of $R_2/R_1 = 2.5$ and an outer cylinder length-to-radius ratio of $L_2/R_2 = 0.5$. Results for two cases, hereby referred to as the *full-hub case* (inner cylinder length = outer cylinder length) and *half-hub case* (inner cylinder length = half the outer cylinder length) are presented here. Results for Rayleigh numbers of 10^4 and 10^6 are explained in detail in each case.

We verified the symmetry condition at the x-z plane by comparing the results for the full geometry with those for the half annulus. The computational domain used in the present study makes use of a variable mesh configuration. We used a fine mesh in regions where steeper gradients were expected, i.e., near all the solid walls and near the open end of the annulus. The mesh was made progressively coarser toward the far-field locations because the field variables were not expected to change by a significant amount in this part of the domain. We determined the mesh size after extensive numerical experiments. A compromise

Table 2 Comparison of mean Nusselt numbers at the top angular plane ($Ra = 4.3 \times 10^3$)

	Mean Nusselt numbers at the top angular plane	
	Inner cylinder	Outer cylinder
FDM	0.70	1.3
FEM	0.715	1.316
Difference (%)	1.71	1.07

between the accuracy and CPU time had to be struck to make our computations cost-effective. For the full-hub geometry, the basic grid structure consisted of 4905 nodes (3968 elements) though these had to be increased to 6865 nodes (6112 elements) for higher Rayleigh numbers. For the half-hub geometry, the basic grid structure consisted of 5855 nodes (5184 elements) for low Rayleigh numbers, while for higher Rayleigh numbers, the grid consisted of 9605 nodes (8672 elements). These mesh configurations resulted in sufficiently fast solutions, without any significant loss of accuracy. In our analysis, we used eight-noded isoparametric brick elements with trilinear velocity and temperature approximations and a discontinuous pressure

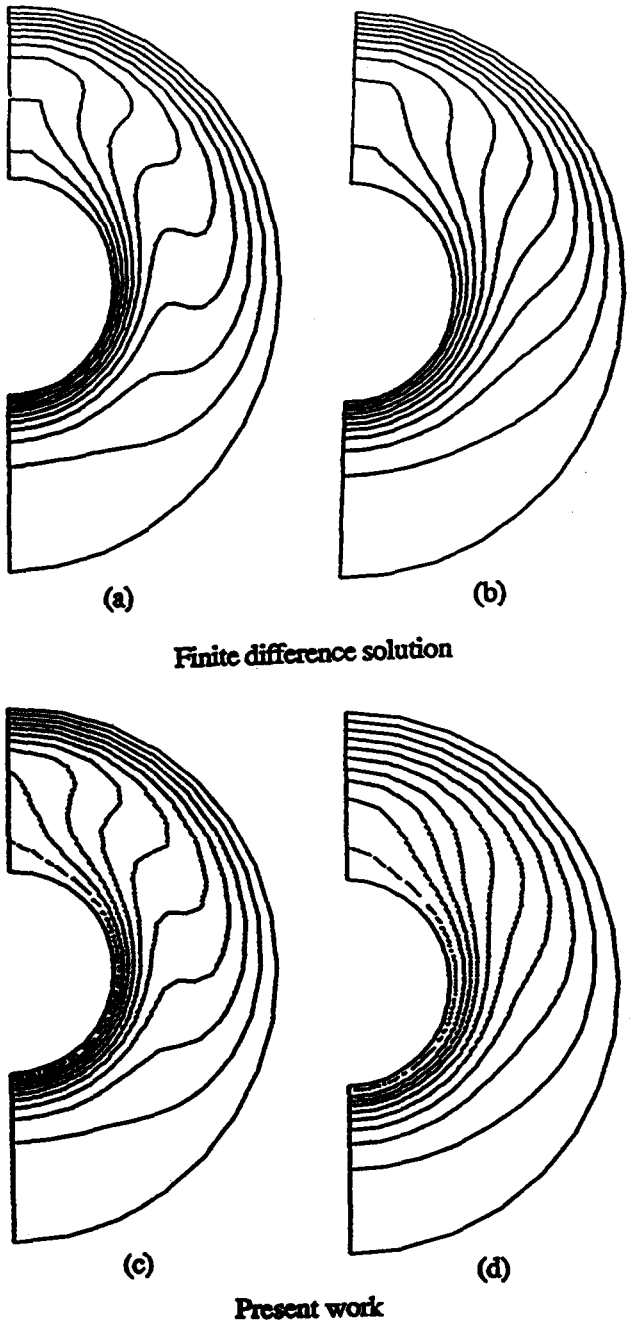

Figure 5 Comparison of isotherms for the closed annulus ($Ra = 4.3 \times 10^4$) at different locations. (a) and (c) Mid-axial plane; (b) and (d) end wall

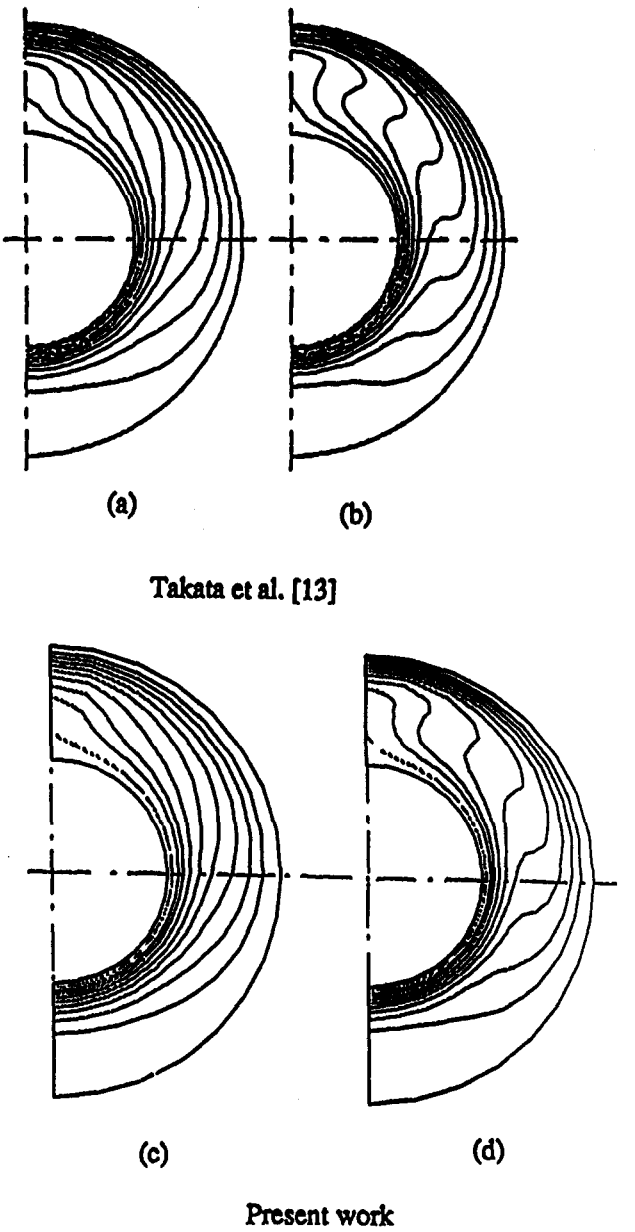

Figure 6 Comparison of isotherms for the closed annulus at different locations ($Ra = 10^5$, $Pr = 5 \times 10^3$). (a) and (c) End wall; (b) and (d) mid-axial plane

approximation. We made some computations using the 27-noded brick elements and found that a higher CPU time was required than that for the eight-noded case, and the results obtained were the same in both cases. Typically, all the simulations were started with a rather conservative estimate of the time step size (0.01–0.05). We established the proper time step size by carrying out extensive numerical experimentation. This is also necessary to understand the evolution of the flow and temperature fields in the early stages of the flow development. The variable time increment algorithm incorporated in the code varies the time step size automatically as the flow evolves and approaches steady state. The computations using FIDAP were performed on the DECstation 5000 workstation and also on the Cray-YMP Supercomputer at the Ohio Supercomputer Center. The CPU time required on the Cray-YMP Supercomputer for converged steady-state solutions was approximately 120 minutes.

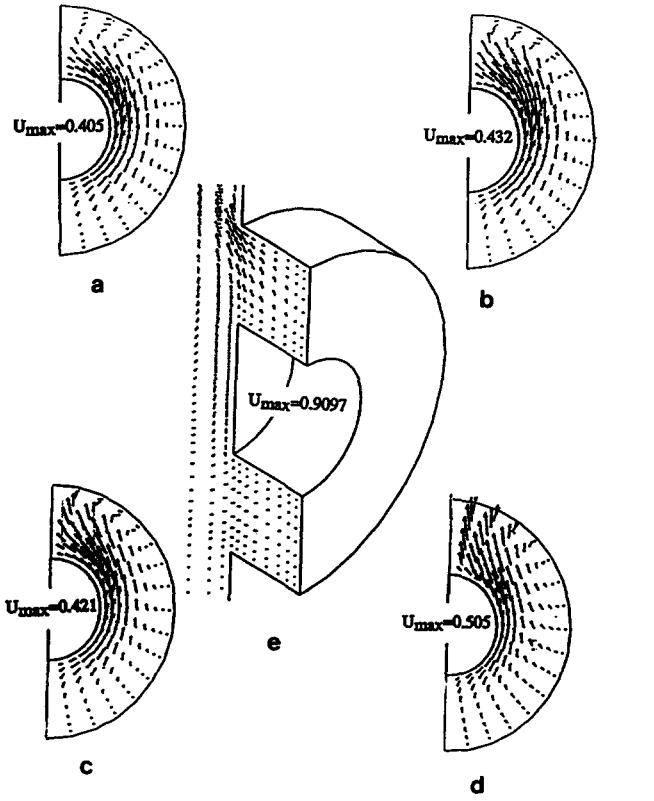

Figure 7 Velocity vector field for $Ra = 10^4$ (full-hub case). (a) $z = L_2/4$; (b) $z = L_2/2$; (c) $z = 3L_2/4$; (d) $z = L_2$ (aperture plane); (e) symmetry plane

Effect of Rayleigh number

Full-hub case ($Ra = 10^4$). The flow field in the symmetry plane and in different cross-stream planes perpendicular to the z-axis of the annulus, separated by distances of one fourth of the annulus length, measured from the solid end wall up to and including the aperture plane, are shown in Figure 7. For brevity, all the flow fields are represented here by means of velocity vectors, and the axial velocity contours are not shown. The velocity vectors are normalized with respect to the highest magnitude of the velocity vector (resultant of the radial and angular components) in that plane. This method of scaling is solely used for clarity of representation. The maximum values of the velocity vectors in the cross-stream planes are indicated in Figure 7. The corresponding maximum axial velocities are 0.05, 0.125, 0.225, and 0.45, whereas the minimum axial velocities are -0.025, -0.075, -0.1, and -0.125, respectively.

As is amply demonstrated by the figures and the values of the axial velocities mentioned above, a complex, 3-D flow field exists in and around the annular cavity. In regions close to the end wall (Figure 7a) of the cavity the basic crescent-shaped flow pattern, characteristic of a 2-D buoyancy-driven flow in an annulus is found to exist, i.e., the fluid rises along the thermal boundary layer along the inner cylinder and after a separation point close to the top of the inner cylinder, rises as a buoyant plume toward the cold outer cylinder. It then moves downward in a boundary layer along the outer cylinder, thus completing the recirculation pattern in the radial plane. The axial component of velocity is so weak at this location that it hardly has any influence on the velocity field in the radial plane. At a location further away from the end wall (Figure 7b), it is observed that the axial velocity is still not strong enough to exhibit any influence on the radial plane velocity distribution. However, because the viscous shearing effect of the end wall is less dominant in this region, velocity values are higher than in the planes closer to the end wall. At the next axial location (Figure 7c), the effects of the open boundary start showing up. The high axial velocities in this region due to the interaction of the fluid with the outside domain through the open end, explain the decrease in magnitude of the velocity vectors in the radial plane.

Finally, at the aperture plane (Figure 7d), the recirculation pattern of the flow field inside the annulus in the x-y plane breaks down. The axial velocities are the highest at the aperture plane. Due to the additional energy gained by the fluid from the heated flat surface of the inner cylinder, the velocity vectors in the aperture plane also have the highest magnitudes. The fluid coming out of the top portion of the cavity meets the fluid rising along the flat surface of the inner cylinder, thus resulting in a buoyant jet ejecting from the top portion of the cavity at a high velocity. The outgoing hot fluid is replaced by a continuous stream of cold fluid from the lower half of the cavity. We also made the following interesting observations from the values of the axial velocities at the aperture plane obtained in our computations. Due to the local suction effect caused by the hot fluid leaving from the top of the cavity, some fluid enters the cavity along the top of the inner cylinder. Similarly, due to a local ejection effect in the lower part of the cavity, an axial convective flow coming out of the cavity is observed around the bottom portion of the inner cylinder.

Figure 8 represents the local Nusselt number values for the full-hub case and $Ra = 10^4$. The three surfaces referenced in this figure are the circumferential surface of the inner cylinder, the flat surface of the inner cylinder (facing the ambient surroundings), and the circumferential surface of the outer cylinder. The Nusselt number here is defined as the dimensionless heat flux, $Nu = q_n = \partial T/\partial n$, where n denotes the outward pointing normal from the surface over which the Nusselt number is to be calculated. This definition of the Nusselt number is used to represent all the heat transfer results in the present study. The Nusselt numbers are plotted at different angular positions chosen such that the variation of heat fluxes over the entire surface can be easily understood. All the angles mentioned in the figures are measured from the bottom angular plane of the annulus. As shown in Figure 8a, for the inner cylinder, the Nusselt numbers are the highest at the bottom and go on decreasing progressively toward the upper surface. This is because of the existence of a very thin thermal boundary layer around the lower half of the inner cylinder. The fluid rises along the thermal boundary layer over the curved surface of the inner cylinder and at some point near the top of the inner cylinder, a boundary-layer separation occurs, resulting in a reduction of the local Nusselt number over the top of the inner cylinder. The Nusselt number remains relatively constant for about two thirds of the annulus length away from the closed end. The influence of the open boundary in enhancing the heat transfer from the inner cylinder can be seen from the figure. At the open end, the value of the Nusselt number experiences an increase of almost 75 percent over its value inside the cavity. This increase in the Nusselt number values is a result of the high axial velocities of the fluid at the open end. As expected, over the flat surface of the inner cylinder (Figure 8b), the heat transfer is maximum over the lower portion and decreases toward the upper angular plane. The local Nusselt numbers over the outer cylinder surface are shown in Figure 8c. The buoyant plume leaving the inner cylinder strikes the top of the outer cylinder, giving the maximum heat transfer rates at this location. The relatively stagnant fluid in the lower region of the cavity explains the minimum values of the heat fluxes at the lowermost positions of the outer cylinder. Once again, the

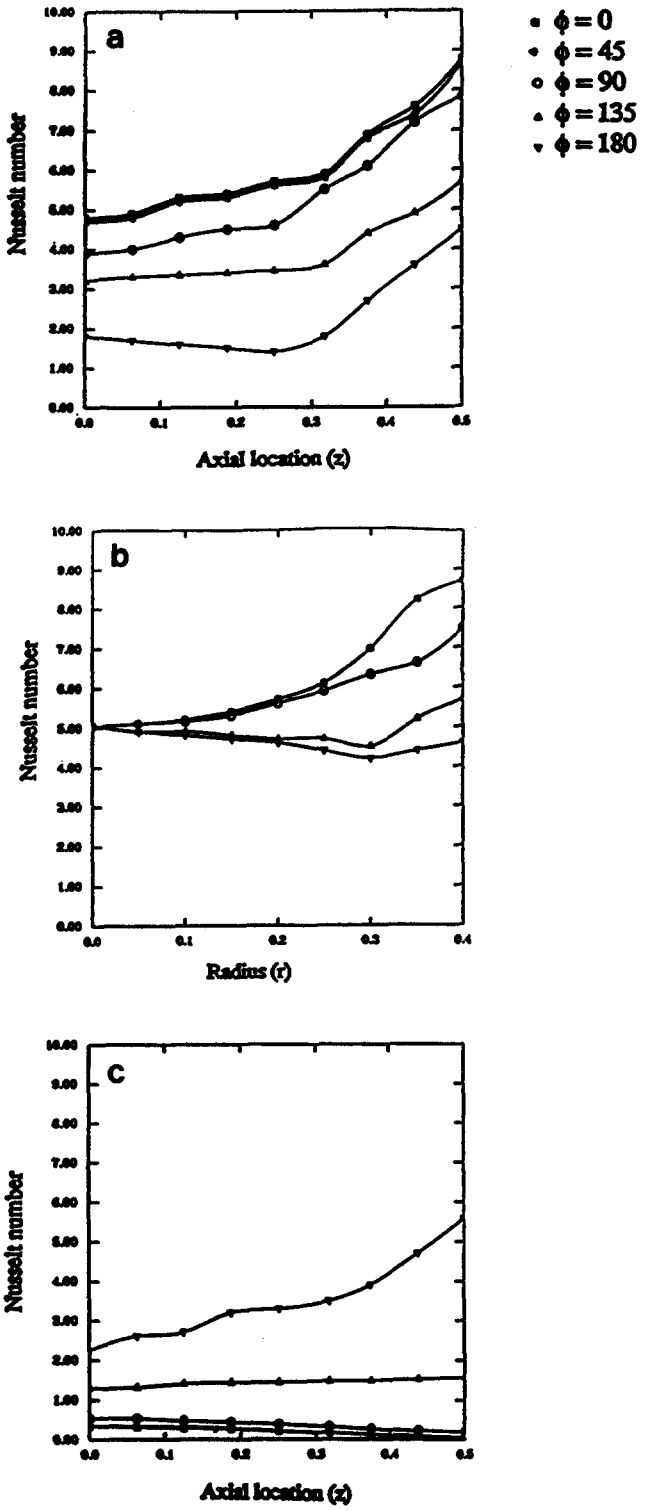

Figure 8 Spatial distribution of the local Nusselt number for Ra = 10^4 (full-hub case). (a) Inner cylinder (curved surface); (b) inner cylinder (flat surface); (c) outer cylinder

drastic increase in the outer cylinder Nusselt number at regions close to the aperture plane is because of the high axial velocities associated with the fluid. Since the fluid is ejected out of the cavity as a buoyant jet along the top surface of the inner cylinder, the heat transfer is greatly enhanced in this region, as can be clearly seen from the figure.

Full-hub case (Ra = 10^6). Figure 9a shows the flow-field pattern at an axial location very close to the rigid end wall of the annulus. Here, the 2-D crescent-shaped recirculation pattern is observed as in the previous case. However, because of the higher Rayleigh number, the associated velocities in the x-y plane as well as the axial velocities are much higher. Also, the boundary-layer effect is more evident in this case as is seen from the concentration of the high velocity vectors close to the cylinder walls. At the next position (Figure 9b), the magnitudes of the axial velocities as well as the velocity vectors in the radial plane increase. This is because the retardation effect of the end wall diminishes in this region. However, at a location further toward the open end (Figure 9c), a decrease in the axial velocity is observed. This region situated approximately between 1/4 to 3/8 of the annulus length measured from the closed end marks a bifurcation zone of the flow field in the cavity and is physically explained as follows.

At high Rayleigh numbers, the interaction of the fluid from the surroundings with the cavity fluid through the open end is stronger. Simultaneously, the strength of the basic crescent-shaped recirculating flow in each of the radial planes of the cavity also increases. This crescent-shaped recirculating flow pattern picks up momentum as it proceeds in a spiral path away from the solid closed end. Meanwhile, the fluid entering the cavity from the open end penetrates into the cavity and approaches this strong recirculating flow approaching the open end. The net effect of the interaction of these two flow fields is to cause an axially stagnant zone in the cavity demarcating two complex 3-D recirculating flows: one is dominant in the axial direction interacting with the ambient through the open end, whereas the other is confined to a region close to the solid end wall. The interaction between these two spirally rotating cells is negligible as far as flow exchange between them is

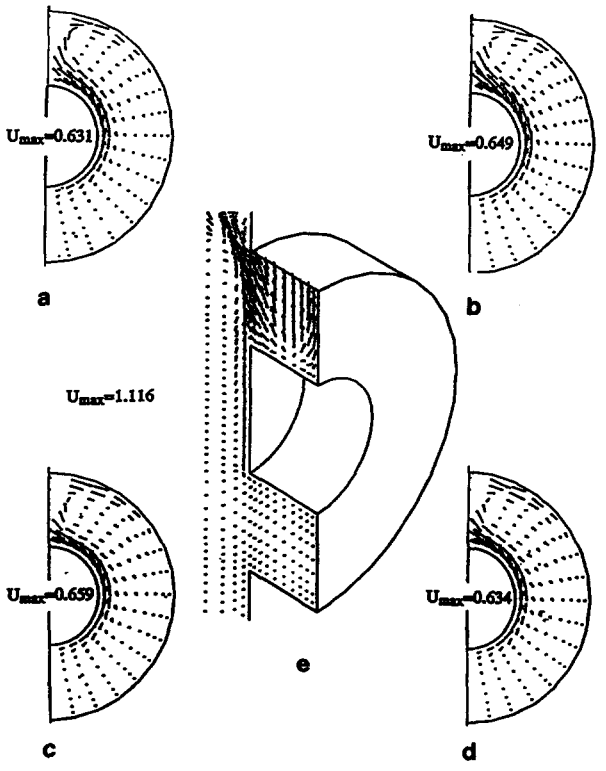

Figure 9 Flow patterns for Ra = 10^6 at different axial positions (full-hub case). (a) $z = L_2/8$; (b) $z = L_2/4$; (c) $z = 3L_2/8$; (d) $z = L_2/2$; (e) velocity vector field at the symmetry plane

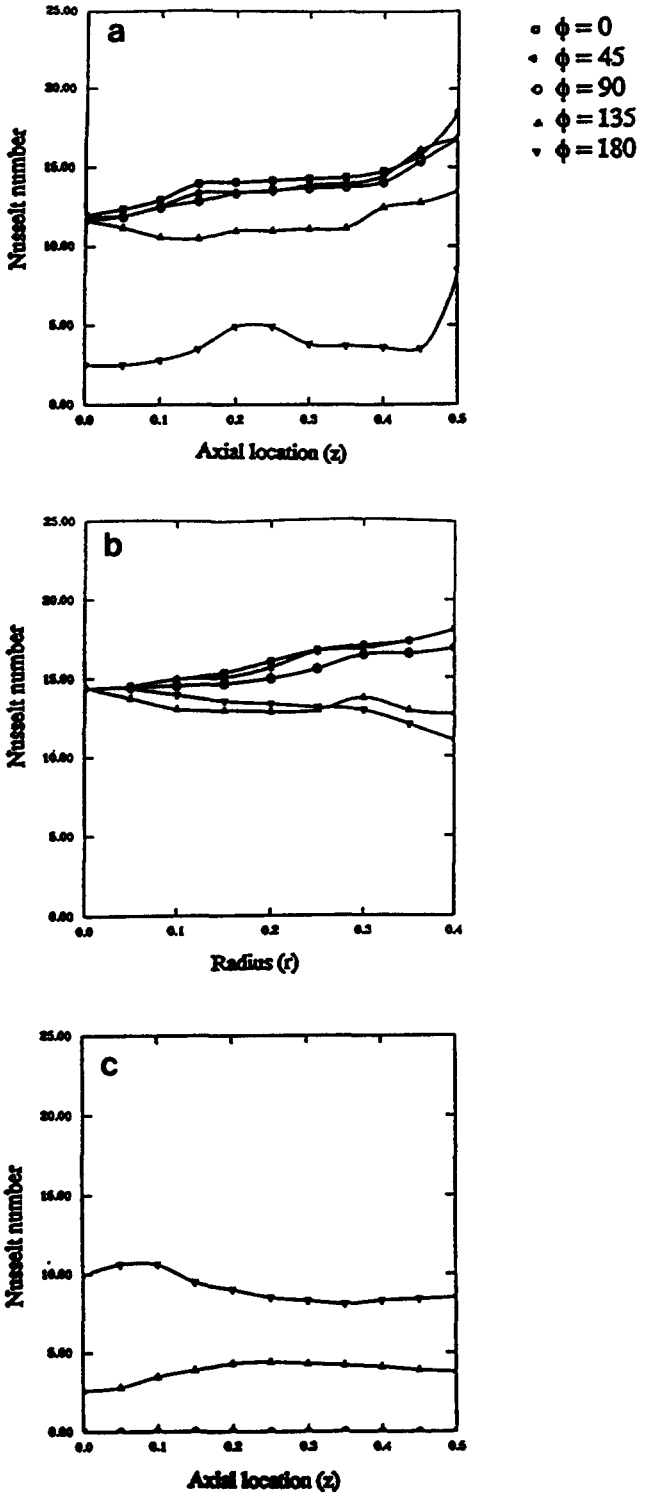

Figure 10 Spatial distribution of the local Nusselt number for Ra = 10^6 (full-hub case). (a) Inner cylinder (curved surface); (b) inner cylinder (flat surface); (c) outer cylinder

concerned. This is well demonstrated by the presence of a small axial velocity component at the dividing plane. This interesting phenomenon is typical for the type of geometries involving an unconfined outer region and a confined inner region. Beyond this plane, due to the penetration of the open boundary effects, the fluid picks up momentum in the axial direction. This can be seen from the values of the axial component of the velocities, which indicate a strong axial convective flow in the region beyond the bifurcation zone and toward the open end of the cavity. Correspondingly, the velocity vectors in the radial planes decrease in magnitude, resulting in a weaker flow in the radial planes. However, in the region very close to the open end, the velocity vectors in the radial planes are much higher because of the energy gained by the fluid from the vertical heated surface of the inner cylinder and also because of the minimal resistance to this flow at the open end. At the aperture plane, the crescent-shaped pattern breaks down completely, resulting in an almost vertical flow at the open end. The velocities at this location are maximum because of the additional energy imparted to the fluid by the hot inner cylinder at the aperture plane.

Figures 10a–c show the heat transfer results for the full-hub case and Ra = 10^6. The influence of the Rayleigh number in enhancing the heat transfer rates can be easily seen from the figure. The overall heat transfer from the three surfaces has increased to approximately twice its value at the lower Rayleigh number. Again, the influence of the open end in increasing the heat transfer rates in the cavity becomes apparent. At the uppermost plane, the wavy nature of the Nusselt number variation is a result of the bifurcation zone explained earlier. In essence, the Nusselt number increases because of the local peak in the radial plane velocities. Near the closed end of the annulus, the strength of the recirculating flow pattern decreases, causing the Nusselt number to decrease. As the fluid approaches the open end, however, the axial velocities pick up magnitude, resulting in an increase in the Nusselt number at the aperture plane. The heat flux over the flat surface of the inner cylinder shows the same nature as in the previous case, except that the magnitudes are much higher because of the higher velocities of the fluid at higher Rayleigh numbers. For the outer cylinder, the heat fluxes are almost zero in the lower region, indicating the existence of a virtually stagnant fluid in the lower part of the cavity. However, the Nusselt numbers are higher over the top half of the outer cylinder due to the high velocity of the fluid striking the top half of the outer cylinder. As can be seen from the figures, the effect of the bifurcation zone on the outer cylinder Nusselt number is not significant. There is a small increase in the Nusselt number values at the aperture plane because, at high Rayleigh numbers, the axial velocities are of the same order of magnitude as the velocities in the radial planes.

Effect of inner cylinder length

The effect of the length of the inner cylinder on the flow and temperature fields in the cavity were investigated by considering the half-hub case in which the length of the inner cylinder is half that of the outer cylinder. We investigated the influence of the change in this geometric parameter thoroughly to determine its importance in optimizing the heat transfer rates in the annular cavity. As mentioned before, in domains of practical interest, such as the brake housing of an aircraft, where this geometry is directly applied to model the wheel outboard portion, the effect of the change in this parameter on the thermal performance could result in significant savings, both in manufacturing and transportation costs. Here, the cavity comprises two parts—the annular gap between the inner and outer cylinders and the cylindrical portion formed by the outer cylinder beyond the region where the inner cylinder ends.

Half-hub case (Ra = 10^4). In order to study the structure of the flow field inside the annulus and also in regions close to the open end, the flow patterns are illustrated at the vertical

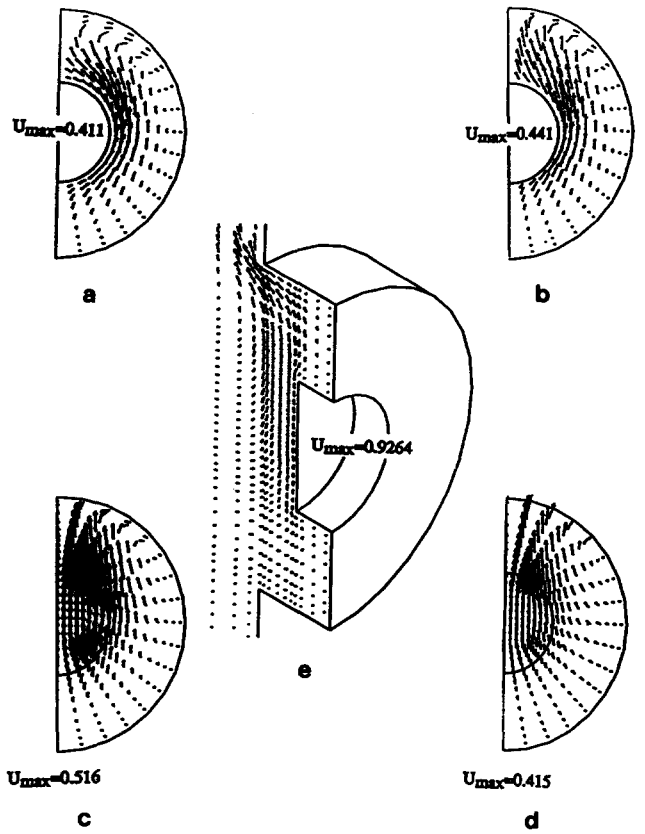

Figure 11 Velocity vector field for Ra = 10^4 (half-hub case). (a) $z = L_2/4$; (b) $z = L_2/2$ (inner cylinder interface); (c) $z = 3L_2/4$; (d) $z = L_2$ (aperture plane); (e) symmetry plane

symmetry plane and in radial planes at four different axial positions one fourth of the outer cylinder length away from the solid end wall (Figure 11), including the two important aperture planes—one at the position where the inner cylinder ends (inner cylinder interface) and the other where the cavity opens into the surroundings (aperture plane). The maximum values of the velocity vectors at these planes are 0.4114, 0.441, 0.5165, and 0.4151, respectively. The magnitudes of the corresponding maximum and minimum axial velocities are 0.062, 0.155, 0.31, and 0.62 and −0.031, −0.093, −0.124, and −0.155, respectively.

Similar to the full-hub case, the basic structure of the flow field is characterized by the bulk of cold fluid entering the cavity from the bottom half and leaving it from the top after having absorbed heat from the hot inner cylinder. Some of the fluid entering the cavity comes in contact with the flat surface of the inner cylinder and as a result of the buoyancy force experienced by it, rises upward along this surface. The remaining fluid moves in the negative axial direction in the bottom portion of the cavity till it reaches the end wall where the axial velocity reduces to zero. At every section in the axial path of the fluid, some of it gets entrained into the recirculating flow field in the radial planes of the annulus. The crescent-shaped recirculation pattern observed in the previous case also exists here. However, there is a considerable difference in the flow field at the plane where the inner cylinder ends and beyond it. At the plane where the inner cylinder ends, two flow-field paths, one caused by the recirculating flow in the annulus and the other due to the fluid particles getting buoyed upward along the flat surface of the inner cylinder mix, resulting in a strong buoyant plume travelling toward the outer cylinder. The flow velocities at this plane are quite strong due to the interaction between the two flow fields. Part of this buoyant fluid, after striking the cold outer cylinder, loses its energy and moves downward along the outer cylinder, thus maintaining a weak recirculation pattern in radial planes beyond the inner cylinder.

However, as a result of the open boundary effects, the remaining buoyant fluid is deflected toward the open end and travels axially toward the open end along the upper portion of the outer cylinder. The magnitude of the velocity vectors at the first aperture plane (Figure 11b) is more than that in a plane closer to the end wall (Figure 11a) because of two effects—the reduction of the retardation effect at the end wall and the additional energy gained by the fluid from the flat surface of the inner cylinder. At the next plane toward the open end (Figure 11c), the velocity vector field becomes stronger because of the persistence of the latter effect in this region and also because the flow resistance has been reduced due to the removal of part of the inner cylinder. At further locations toward the open end, however, the velocities decrease continuously because the driving force to sustain the flow in the radial plane reduces at these locations. The magnitudes of the axial velocities continuously increase toward the open end. As a result, the crescent-shaped recirculation pattern that is observed in the radial planes inside the cavity weakens and finally, the fluid leaves the open end as a buoyant jet with a strong axial velocity component. The velocity field in the vertical symmetry plane (Figure 11e) further verifies this behavior.

The immediate effect of the reduction of the inner cylinder length can be easily noted from these figures. Due to the removal of half of the inner cylinder as compared with the previous case, the resistance to the flow entering the cavity through the open end is considerably reduced. Hence, the overall strength of the flow field, particularly in the axial direction, is significantly higher (except at the symmetry plane) as can be observed from a comparison of the values obtained in this case to those in the full-hub case for the same Rayleigh number. The effect of moving the heated surface inside the cavity causes a larger penetration of the outside fluid into the cavity as is clearly indicated by the presence of strong axial components of velocity in regions well inside the cavity. Just by observing the nature of the flow field, higher heat transfer rates are expected to occur in the case when the inner cylinder is shorter than the outer cylinder.

The Nusselt number variations over the cavity surfaces for the half-hub case and Rayleigh number of 10^4 are shown in Figure 12. The distribution of Nusselt numbers is similar to the full-hub case. However, the values of the Nusselt numbers are much higher than the full-hub case. This is a very important result from the heat transfer point of view and can be used as one method for enhancing the heat transfer coefficients associated with the convective flow in the annular cavity. As the length of the inner cylinder is decreased, the fluid entering the cavity experiences less resistance to flow until it reaches the inner cylinder. By the time it has reached this location inside the cavity, the velocity of the fluid has increased by a sufficient amount. The high velocity fluid then comes in contact with the hot inner cylinder surfaces. Hence, the overall velocities of the flow in and around the cavity are higher than the previous case. This results in higher heat transfer rates from the inner and outer cylinders. Once again, the Nusselt number magnitudes increase by 75 percent over its value inside the cavity.

Half-hub case (Ra = 10^6). The flow field for this geometry and Ra = 10^6 is shown in Figure 13. In this case the convection effects in the symmetry plane are mostly confined to the top half of the cavity while the bulk of the fluid in the lower half of the cavity is virtually stagnant. The confinement of the

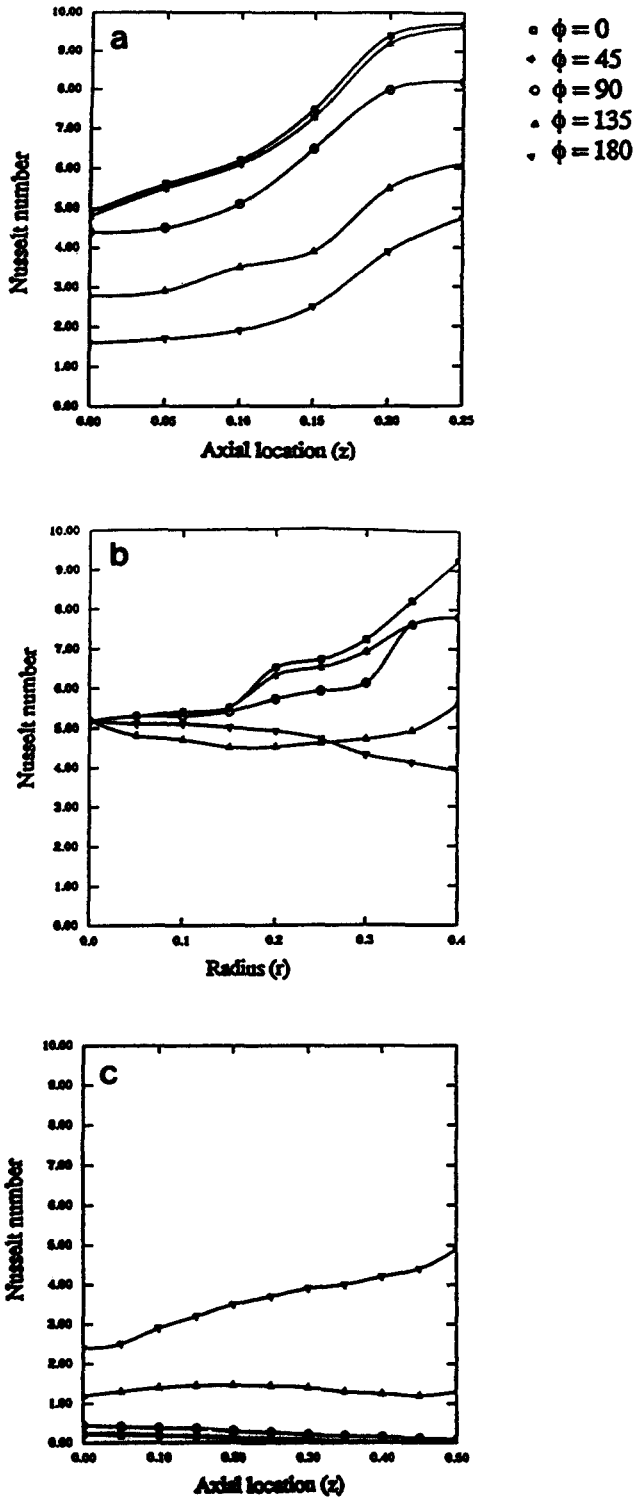

Figure 12 Spatial distribution of the local Nusselt number for Ra = 10^4 (half-hub case). (a) Inner cylinder (curved surface); (b) inner cylinder (flat surface); (c) outer cylinder

viscous effects in a thin boundary layer near the inner and outer cylinders due to the higher Rayleigh number is obvious from the velocity vector field shown in Figure 13. Also, the axial velocities of the outgoing fluid are very high compared with the velocities of the fluid coming in, and, therefore, the region of the annulus occupied by the fluid with a positive axial velocity component is much less than that occupied by the incoming fluid. Comparison of the magnitudes of the velocities for this Rayleigh number with the full-hub case further clarifies the presence of a stronger velocity field for the half-hub case. Furthermore, comparison of the velocity magnitudes in the vicinity of the flat surface of the inner cylinder reveals the presence of a stronger velocity field along the flat surface of the inner cylinder in the half-hub case. Also, reduction in the inner cylinder length shifts the stagnant bifurcation zone further inside the cavity. This is an important result since it shows that the overall heat transfer from the cavity to the surrounding fluid is enhanced due to a smaller stagnation zone.

At higher Rayleigh numbers, for the half-hub case, the heat transfer rates are again higher than for the full-hub case with the same Rayleigh number (Figure 14). This is because of the same reason alluded to earlier. Due to the smaller length of the inner cylinder, the effect of the bifurcation zone on the inner cylinder Nusselt number is not distinguishable in this case. Thus, the inner cylinder Nusselt number is almost constant throughout the length of the cavity and only experiences a distinct jump at the open end because of the higher axial velocities there. Over the lower half of the outer cylinder, the heat transfer coefficients are almost negligible, indicating the stagnation zone of the cavity. Most of the fluid flow activity is confined to the upper portion of the cavity and this is also seen from the significantly higher heat transfer rates over the upper half of the outer cylinder. The effect of the end wall in reducing the strength of the recirculating flow in the cavity is even more pronounced in this case as can be seen from the lower heat flux values at the closed wall. The outer cylinder Nusselt number increases toward the bifurcation zone and then decreases

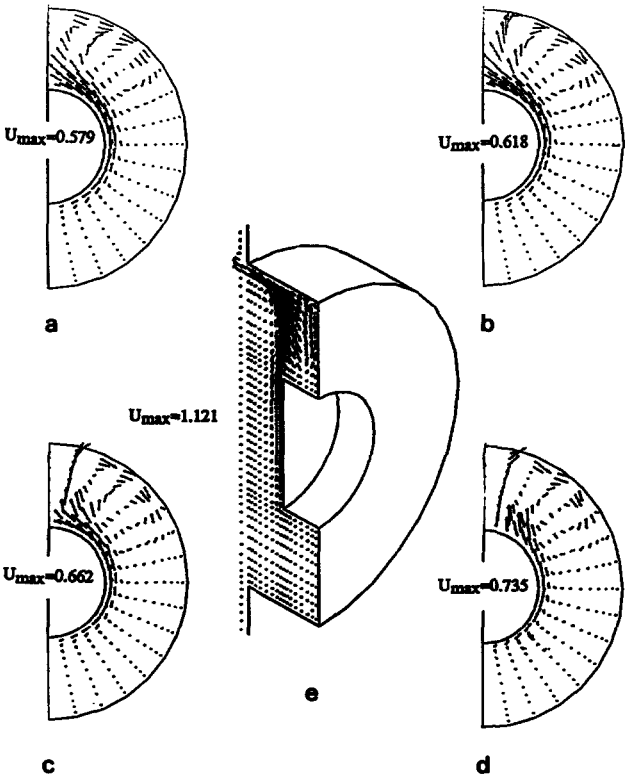

Figure 13 Flow patterns for Ra = 10^6 at different axial positions (half-hub case). (a) $z = L_2/8$; (b) $z = L_2/4$; (c) $z = 3L_2/8$; (d) $z = L_2/2$ (inner cylinder interface); (e) velocity vector field at the symmetry plane

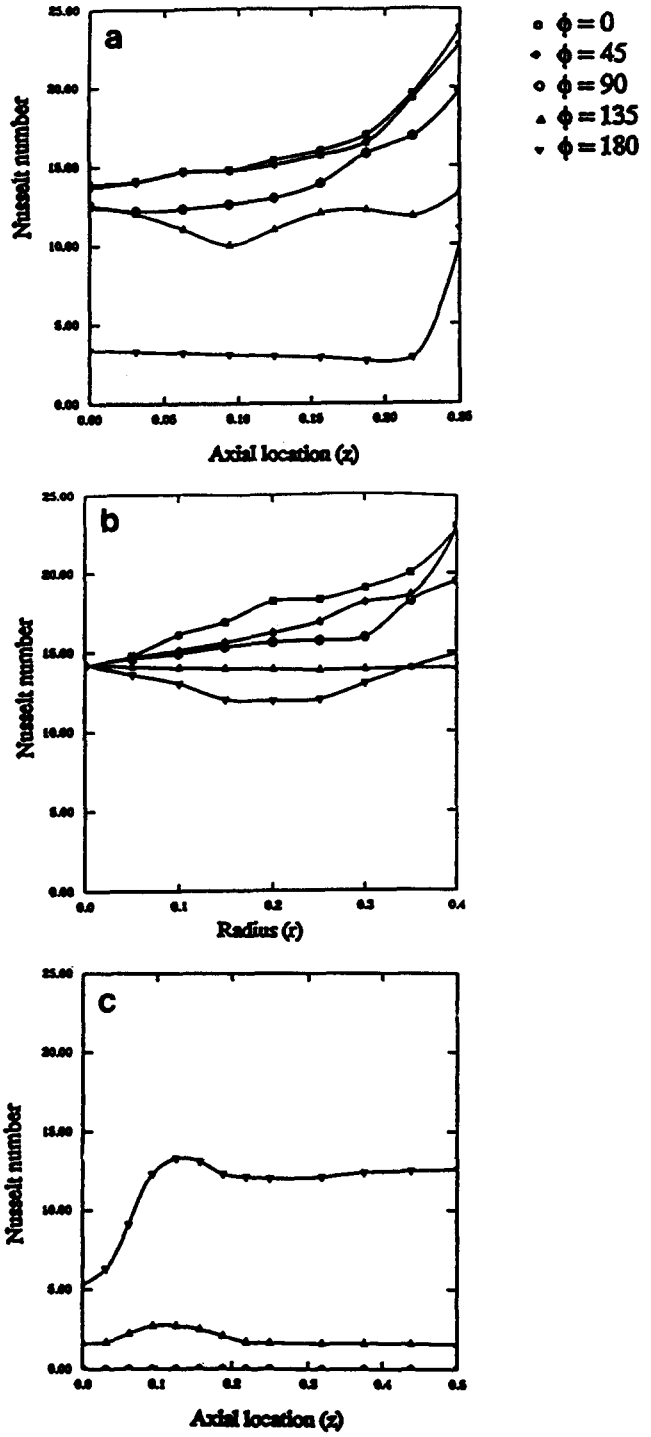

Figure 14 Spatial distribution of the local Nusselt number for $Ra = 10^6$ (half-hub case). (a) Inner cylinder (curved surface); (b) inner cylinder (flat surface); (c) outer cylinder

toward the open end, attaining a constant value, thus indicating the lesser influence of the open end on the outer cylinder Nusselt number in this case. This is because the axial velocities are of the same order of magnitude as the radial plane velocities.

Conclusions

Buoyancy-induced flow and heat transfer in partially open annuli resulting from the sudden heating of the inner cylinder is numerically studied in this work. A detailed study of the 3-D structure of the flow field and heat transfer characteristics within this type of geometry has been carried out. The effect of the open boundary combined with the closed wall of the annulus on the complex 3-D structure of the flow field and heat transfer has been investigated. The influence of the length of the inner cylinder on the flow and heat transfer in and around the cavity has been studied. The numerical results have been obtained for Rayleigh numbers of 10^4 and 10^6. Some of the main contributions of this study are the following:

(1) The open end causes a considerable enhancement in the heat transfer characteristics of the cavity in the vicinity of the open end as is evident from the heat transfer results presented here. The numerical results show the complex interactions of the ambient surrounding with the flow field inside the cavity.

(2) Reduction of the length of the inner cylinder causes higher heat transfer rates from the inner cylinder. At higher Rayleigh numbers, the bifurcation zone is pushed further into the cavity and closer to the end wall, thus causing a better interaction of the ambient fluid with the cavity, resulting in an enhancement of the heat transfer from the inner cylinder.

(3) At low Rayleigh numbers, the effect of the closed-end wall is to retard the flow coming into the cavity through the aperture plane. However, at high Rayleigh numbers, the closed-end wall causes the formation of two spirally rotating cells inside the cavity, separated by an axially stagnant flow region.

Acknowledgment

The support by B. F. Goodrich and the Ohio Supercomputer Center is acknowledged and appreciated.

References

1 Kuehn, T. H. and Goldstein, R. J. An experimental and theoretical study of natural convection in the annulus between horizontal concentric cylinders. *J. Fluid Mech.*, 1976, **74**, 695–719

2 Tsui, Y. T. and Tremblay, B. On transient natural convection heat transfer in the annulus between concentric, horizontal cylinders with isothermal surfaces. *Int. J. Heat Mass Transfer*, 1984, **27**, 103–111

3 Powe, R. E., Carley, C. T. and Carruth, S. L. A numerical solution for natural convection in cylindrical annuli. *ASME J. Heat Transfer*, 1971, **92**, 210–220

4 Ozoe, H., Okamoto, T. and Churchill, S. W. Natural convection in a vertical annular space heated from below. *Heat Transfer Jpn. Res.*, 1979, **8**, 82–93

5 Ozoe, H., Shibata, T. and Churchill, S. W. Natural convection in an inclined circular cylindrical annulus heated and cooled on its end plates. *Int. J. Heat Mass Transfer*, 1981, **24**, 727–737

6 Takata, Y., Iwashige, K., Fukuda, K. and Hasegawa, S. Three-dimensional natural convection in an inclined cylindrical annulus. *Int. J. Heat Mass Transfer*, 1984, **27**, 747–754

7 Fusegi, T. and Farouk, B. A three-dimensional study of natural convection in an inclined cylindrical annulus. *Proc. Eighth International Heat Transfer Conference*, 1986, **4**, 1575–1580

8 Rao, Y., Miki, Y., Fukuda, K., Takata, Y. and Hasegawa, S. Flow patterns of natural convection in horizontal concentric annuli. *Int. J. Heat Mass Transfer*, 1988, **31**, 695–707

9 Fukuda, K., Miki, Y. and Hasegawa, S. Analytical and experimental study on turbulent natural convection in a horizontal annulus. *J. Heat Mass Transfer*, 1990, **33**, 629–639

10 Penot, F. Numerical calculation of two-dimensional natural convection in isothermal open cavities. *Numerical Heat Transfer*, 1982, **5**, 421–437

11 LeQuere, O., Humphrey, J. A. C. and Sherman, F. S. Numerical calculation of thermally driven two-dimensional unsteady laminar flow in cavities of rectangular cross section. *Numerical Heat Transfer*, 1981, **4**, 249–283

12 Ettefagh, J. and Vafai, K. Natural convection in open-ended cavities with a porous obstructing medium. *Int. J. Heat Mass Transfer*, 1988, **31**, 673–693

13 Vafai, K. and Ettefagh, J. Thermal and fluid flow instabilities in buoyancy-driven flows in open-ended cavities. *Int. J. Heat Mass Transfer*, 1990, **33**, 2329–2344

14 Chan, Y. L. and Tien, C. L. A numerical study of two-dimensional natural convection in square open cavities. *Numerical Heat Transfer*, 1985, **8**, 65–80

15 Taylor, C. and Hood, P. A numerical solution of the Navier-Stokes equations using the finite element technique. *Computational Fluids*, 1973, **1**, 73–89

16 Gresho, P. M., Lee, R. L. and Sani, R. L. On the time-dependent solution of the incompressible Navier-Stokes equations in two and three dimensions. *Recent Advances in Numerical Methods in Fluids*, Pineridge, Swansea, UK, 1980

17 *FIDAP Theoretical Manual*, Fluid Dynamics International, Evanston, IL, USA, 1991

18 Engelman, M. S., Strang, G. and Bathe, K. J. The application of quasi-Newton methods in fluid mechanics. *Int. J. Numerical Methods Eng.*, 1981, **17**, 707–718

19 Vafai, K. and Ettefagh, J. An investigation of transient three-dimensional natural convection in a horizontal annulus. *Int. J. Heat Mass Transfer*, 1991, **34**, 2555–2570

20 Vafai, K. and Ettefagh, J. The effects of axial transport on transient natural convection inside of an open-ended annulus. *J. Heat Transfer*, 1991,**113**, 627–634

21 Vafai, K. and Desai, C. A comparative analysis of the finite element and finite difference methods for simulation of buoyancy induced flow and heat transfer in closed and open-ended annular cavities. *Numerical Heat Transfer, Part A* 1992, in press